Field-based angle-resolved light-scattering study of single live cells

Wonshik Choi,[1,*] Chung-Chieh Yu,[1] Christopher Fang-Yen,[1] Kamran Badizadegan,[1,2] Ramachandra R. Dasari,[1] and Michael S. Feld[1]

[1]G. R. Harrison Spectroscopy Laboratory, Massachusetts Institute of Technology, Cambridge, Massachusetts 02139, USA

[2]Department of Pathology, Harvard Medical School and Massachusetts General Hospital, Boston, Massachusetts 02114, USA

*Corresponding author: wonshik@mit.edu

Received April 3, 2008; revised May 23, 2008; accepted May 26, 2008; posted June 16, 2008 (Doc. ID 94664); published July 14, 2008

We perform field-based angle-resolved light-scattering measurements from single live cells. We use a laser interferometer to acquire phase and amplitude images of cells at the image plane. The angular scattering spectrum is calculated from the Fourier transform of the field transmitted through the cells. A concurrent 3D refractive index distribution of the same cells is measured using tomographic phase microscopy. By measuring transient increases in light scattering by single cells during exposure to acetic acid, we correlate the scattering properties of single cells with their refractive index distributions and show that results are in good agreement with a model based on the Born approximation. © 2008 Optical Society of America

OCIS codes: 120.3180, 170.3880.

A number of recent studies have examined light-scattering properties of cells and tissues, often guided by the goal of developing new optical techniques for disease diagnosis. A commonly employed strategy is to use light scattering to characterize size distributions of cell nuclei [1–4], which are known to be enlarged in cells in precancerous lesions [5]. Angularly resolved light scattering is also used to assess subcellular morphology by sizing other smaller organelles, such as mitochondria and lysosomes [6,7]. Conventional light-scattering techniques measure the light-scattering intensity at the Fourier plane (or scattering plane) of the object. Since cells are nearly transparent at visible wavelengths, the scattered intensity is mainly forward directed and is very weak at large scattering angles. This limits the information obtained using intensity-based techniques to study light scattering from single cells. We present a new, field-based technique in which we measure the full electric field, both amplitude and phase, of the scattered light. We record the E field not at the Fourier plane but at the image plane, where the distribution of intensity is quite even owing to the transparent property of cells. By taking the numerical Fourier transform of the E-field image, we obtain the angle-resolved light-scattering distribution. In the following study, we demonstrate that field-based light scattering is capable of measuring the light-scattering distribution of single cells over a wide range of angles with high dynamic range.

We used tomographic phase microscopy (TPM) [8] (Fig. 1) for concurrent measurements of angle-resolved light scattering and refractive index distributions in single cells and for studying the quantitative connection between them. A He–Ne laser beam ($\lambda = 633$ nm) is divided into sample and reference arm paths by a beamsplitter (BS1). In the sample arm, a tilting mirror controlled by a galvanometer (HS-15, Nutfield Technology) is installed to scan the angle of illumination. An infinity-corrected, oil-immersion objective lens (Olympus UPLSAPO 100XO, 1.4 NA) and a tube lens (L2, $f = 200$ mm) are used to image the sample with magnification of 110. In the reference arm, the laser beam passes through two acousto-optic modulators (AOMs) in such a way that the total reference-beam frequency shift is 1250 Hz. A beam splitter (BS2) recombines the sample and reference laser beams, forming an interference image at the camera plane. A high-speed CMOS camera (Photron 1024PCI) records four images separated by 200 μs, exactly one-fourth the reciprocal of the heterodyne frequency. In this way, four interference patterns I_1, I_2, I_3, and I_4, are recorded, in which the sample-reference phase shift is increased by $\pi/2$ between consecutive images. Then, by applying phase-shifting inteferometry, the phase $\phi_S(x,y)$ and amplitude

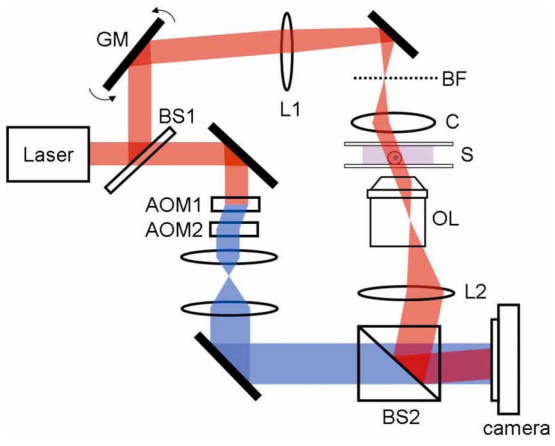

Fig. 1. (Color online) Schematic diagram of tomographic phase microscope: GM, galvanometer scanning mirror; L1, focal length $f = 250$ mm lens; BF, backfocal plane of the condenser lens; C, condenser lens; S, sample; OL, objective lens; L2, $f = 200$ mm lens; AOM1 and 2, acousto-optic modulators; BS1 and 2, beam splitters. The frequency-shifted reference laser beam is shown as darkned after AOM.

$A_S(x,y)$ are obtained from the relation $\phi_S(x,y) = \arg z_S(x,y)$ and $A_S(x,y) = \mathrm{abs}[z_S(x,y)]$, with $z_S(x,y) = (I_4 - I_2) + i\,(I_3 - I_1)$ [9].

A 3D map of refractive index was obtained with the same method described in the previous publication [8]. The angular light-scattering distribution was measured from phase and amplitude images taken at angle of illumination zero. Background phase and amplitude images were also collected for aberration compensation. We use the normalized amplitude $A(x,y) = A_S(x,y)/A_B(x,y)$ and background-subtracted phase $\phi(x,y) = \phi_S(x,y) - \phi_B(x,y)$ to calculate the background-corrected electric field $E(x,y) = A(x,y)\exp(i\phi(x,y))$. We then calculate the spatial Fourier transform of this field, $\tilde{E}(\nu_x, \nu_y)$ with ν_x and ν_y the spatial frequencies conjugate to x and y. $\tilde{E}(\nu_x, \nu_y)$ corresponds to the field at the Fourier plane of the image. Since the wavelength of the source is conserved after the scattering, the spatial frequencies (ν_x, ν_y) can be expressed as polar angle σ and azimuth angle ψ via the relations $\sigma = \sqrt{\nu_x^2 + \nu_y^2} = n\sin(\sigma)/\lambda$ and $\psi = \arctan(\nu_y/\nu_x)$, respectively, with n the refractive index of the medium and λ the wavelength of the source. We then acquire the angular light-scattering distribution $I_s(\sigma)$ only as a function of polar angle σ by averaging $|\tilde{E}(\nu_x, \nu_y)|^2$ over ψ.

To validate our technique, we imaged a sample composed of a 10 μm diameter polystyrene bead (Polyscience) in immersion oil (Cargille, series A; refractive index 1.56). Amplitude $A(x,y)$ and phase $\phi(x,y)$ images of one bead are shown in Figs. 2(a) and 2(b). The angular scattering distribution, $|\tilde{E}(\nu_x, \nu_y)|^2$, is shown in Fig. 2c. The index tomogram of a 10 μm bead was presented in our previous publication [10].

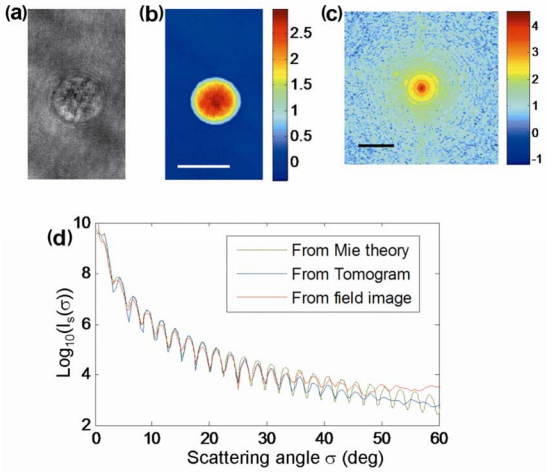

Fig. 2. (Color online) Angular distribution of light scattering for a 10 μm polystyrene bead: (a) amplitude image of the bead, (b) quantitative phase image of the bead (the scale bar indicates 10 μm, and the color bar indicates the phase in radians); (c) angular scattering distribution, $|\tilde{E}(\nu_x, \nu_y)|^2$ (the 1 μm^{-1} scale indicates the base-10 logarithm of the intensity); and (d) angular scattering distribution obtained from Mie theory (dashed-dotted curve), tomogram (dotted curve) and field image (solid curve), respectively.

Figure 2d compares the measured angular scattering distribution, $I_s(\sigma)$, from the E-field image (solid curve) with the distribution predicted by Mie theory (dashed-dotted curve) for scattering from a dielectric sphere with diameter and index contrast corresponding to the experiment. For most of the range of scattering angles there is an excellent agreement between theory and experiment for both the frequency of oscillations and the fall-off with angle. Note that the scattering distributions presented here exhibit more than 5 orders of magnitude of variation for a single bead with single measurement. Such a large dynamic range is possible because the measurement is performed at the image plane, where the light intensity is roughly constant, rather than directly at the Fourier plane, where measurement would be limited by the dynamic range of the optical system and detector.

We can also numerically obtain the angular distribution of light scattering from the refractive index tomogram measured by TPM. For samples with complex refractive index distributions, including cells, numerical methods are required. Under the Born approximation, valid for samples that induce relatively small phase shifts [11], the Fourier transform of the scattered field, $E_s(x,y)$, is related to the Fourier transform of scattering potential, $O(x,y,z) = -(2\pi/\lambda)^2(n^2(x,y,z) - n_m^2)$, with $n(x,y,z)$ the complex refractive index at the specimen and n_m the refractive index of the medium, by the following relation [12]:

$$\tilde{E}_s(\nu_x, \nu_y) = \frac{\pi}{i\sqrt{\nu_0^2 - \nu_x^2 - \nu_y^2}}\tilde{O}(\nu_x, \nu_y, \sqrt{\nu_0^2 - \nu_x^2 - \nu_y^2} - \nu_0),$$

where $\tilde{O}(\nu_x, \nu_y, \nu_z)$ and $\tilde{E}_s(\nu_x, \nu_y)$ are the Fourier transforms of $O(x,y,z)$ and $E_s(x,y)$, respectively, and $\nu_0 = 1/\lambda$.

We used the Born approximation to calculate the angular scattering profile from the refractive index distribution of the bead as determined by TPM. Figure 2d shows a comparison of the calculated profile (dotted curve) and the experimentally measured scattering distribution (solid curve). Note that no extra fitting parameter was used to mach the amplitudes, since we normalized the amplitude of the sample field in the experiment. Excellent agreement is obtained for angles less than 45 deg.

After validating these methods with beads as described, we carried out similar measurements in live HeLa cells. In addition, we performed these measurements before and after exposing the cells to acetic acid. Cells were dissociated from culture dishes and incubated for 4–5 h in imaging chambers as previously described [8] so that individual cells become attached to their glass substrates. We obtained refractive index tomograms before and after changing the cell environment from a normal culture medium [Fig. 3(a)] to a culture medium containing 0.5% acetic acid [Fig. 3(b)] and then back to normal [Fig. 3(c)]. Figure 3(d) shows the angular scattering distributions measured at each step.

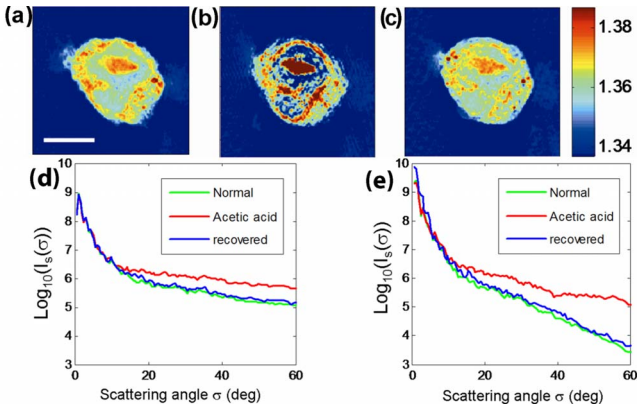

Fig. 3. (Color online) Angular-scattering distribution for a live HeLa cell: (a) refractive index tomograms in normal culture medium; (b) medium containing 0.5% acetic acid and (c) after replacing the original culture medium; (d) angular-scattering distributions, $I_s(\sigma)$, measured from the field image under three different conditions; and (e) angular-scattering distributions calculated from refractive index tomograms [(a)–(c)] measured by TPM.

After adding acetic acid, the refractive index of the nucleolus increased from 1.36 to 1.40, and the heterogeneity of the rest of the nucleus and cytoplasm increased dramatically. The angular scattering distribution measured from the E-field image exhibited a dramatic increase in scattering for angles greater than 10 deg [Fig. 3(d)]. One minute after replacing the acetic acid medium with the normal culture medium, the spatial variation in refractive index decreased [Fig. 3(c)] but remained slightly larger than its baseline value. Similarly, the cell light scattering nearly recovered its original distribution [Fig. 3(d)].

To connect structural changes of the cells with the angular light-scattering distributions, we calculated the forward angular scattering distribution [Fig. 3(e)] of HeLa cells from their refractive index tomograms [Figs. 3(a)–3(c)] using the Born approximation. These calculations indicate an increase in scattered light at large angles after adding acetic acid, especially at angles larger than 10 deg, in agreement with the angular scattering measurements [Fig. 3(d)]. The Born approximation provides a means of quantitatively relating the Fourier transform of the refractive index map to the angular-scattering distribution. In this way, we connect spatial frequency of the refractive index structure to scattering angle. High spatial-frequency structures will contribute to large angle scattering. The scattering angle of 10 deg corresponds to the spatial frequency of $1/3\ \mu m^{-1}$. Therefore, our analysis verifies that increase in structures finer than 3 μm by the addition of acetic acid is responsible for the increase in large angle scattering. There are discrepancies between the angular scattering measurements [Fig. 3(d)] and the Born approximation calculation from the 3D index tomograms [Fig. 3(e)] at angles larger than 30 deg. This is due to the reduced spatial resolution in 3D reconstruction of tomograms introduced by the projection approximation [10]. By developing a 3D reconstruction algorithm that incorporates diffraction, we will be able to reduce or eliminate these discrepancies.

This work presents to our knowledge the first quantitative comparison between the 3D refractive index map of a single cell and its angular light-scattering spectrum. By perturbing the scattering properties of a single cell, we directly observe the increase in light scattering at large angles induced by an increased heterogeneity of the refractive index map. Of particular interest will be the elucidation of contributions to scattering from subcellular organelles.

This work was funded by the National Institutes of Health (P41-RR02594-18), the National Science Foundation (DBI-0754339) and Hamamatsu Corporation.

References

1. V. Backman, R. Gurjar, K. Badizadegan, L. Itzkan, R. R. Dasari, L. T. Perelman, and M. S. Feld, IEEE J. Sel. Top. Quantum Electron. **5**, 1019 (1999).
2. C. C. Yu, C. Lau, J. W. Tunnell, M. Hunter, M. Kalashnikov, C. Fang-Yen, S. F. Fulghum, K. Badizadegan, R. R. Dasari, and M. S. Feld, Opt. Lett. **31**, 3119 (2006).
3. K. Sokolov, R. Drezek, K. Gossage, and R. Richards-Kortum, Opt. Express **5**, 302 (1999).
4. T. T. Wu, J. Y. Qu, and M. Xu, Opt. Lett. **32**, 2324 (2007).
5. V. Kumar, A. K. Abbas, and N. Fausto, *Robbins & Cotran Pathologic Basis of Disease*, 7th ed. (2005).
6. J. D. Wilson and T. H. Foster, J. Biomed. Opt. **12**, 030503 (2007).
7. J. R. Mourant, J. P. Freyer, A. H. Hielscher, A. A. Eick, D. Shen, and T. M. Johnson, Appl. Opt. **37**, 3586 (1998).
8. W. Choi, C. Fang-Yen, K. Badizadegan, S. Oh, N. Lue, R. R. Dasari, and M. S. Feld, Nat. Methods **4**, 717 (2007).
9. K. Creath, Prog. Opt. **26**, 349 (1988).
10. W. Choi, C. Fang-Yen, K. Badizadegan, R. R. Dasari, and M. S. Feld, Opt. Lett. **33**, 171 (2008).
11. A. C. Kak, and M. Slaney, *Principles of Computerized Tomographic Imaging* (Academic, New York, 1999).
12. E. Wolf, Opt. Commun. **1**, 153 (1969).